Available online at www.CivileJournal.org

Civil Engineering Journal

(E-ISSN: 2476-3055; ISSN: 2676-6957)

Vol. 9, No. 05, May, 2023

Study of the Effect of Magnetic Field on Dispersion of Crushed Portland Cement and Tensile Strength of Cement Stone

Ruslan Ibragimov [1*], Evgenij Korolev [2], Evgeny Khorkov [1], Linur Gimranov [1]

[1] *Kazan State University of Architecture and Engineering, Zelenaya Street 1, 420043 Kazan, Russian Federation.*

[2] *Saint Petersburg State University of Architecture and Civil Engineering, St. Petersburg, Russian Federation.*

Received 25 January 2023; Revised 19 April 2023; Accepted 24 April 2023; Published 01 May 2023

Abstract

This paper investigates the effect of a magnetic field on the grinding processes of Portland cement and the axial tensile strength of cement stone. It was found that the dispersion composition of Portland cement is affected by the magnetic field in two modes. Moreover, the grinding of Portland cement without a magnetic field has subtle modes within small particles (0.1–0.4 microns). The grinding of Portland cement with a magnetic field demonstrates an increase in the mode area of small particles and a decrease in the area of large particles (more than 1.6 microns), with an increase in processing time. In this work, the previously established magnetoplastic effect was confirmed in cement stone only in crystalline samples. The determined effect on cement stone is to reduce its strength by 53-59% and simultaneously increase relative deformation by 63–149%, depending on the specimen size and type. The magnetoplastic effect is also visually recorded on scans of the crack edges in cement stone examined using probe microscopy. The obtained experimental data confirm the validity of the proposed hypothesis of the effect of the magnetic field on polycrystalline materials with isotropic structure, in particular portland cement and cement stone, which consists in the fact that the magnetic field contributes to the accumulation of dislocations in the material, an acceleration of their movement, and the development of cracks.

Keywords: Electromagnetic Mill; Magnetic Field; Deformation; Energy Consumption; Magnetoplastic Effect; Cement Stone.

1. Introduction

Currently, around 2.4 billion tons of CO_2 are released into the atmosphere when Portland cement is produced around the world. Herewith, the production of Portland cement is extremely energy-intensive: the consumption of fuel equivalent for firing 1 ton of clinker amounts to 215 kg; electricity for grinding the same is 119 kWh [1]. Hence, it is natural that we search for technological solutions to reduce the amount of portland cement used in cement or to reduce the energy consumption during grinding.

One of the most effective methods of grinding Portland cement is the use of an electromagnetic mill, which has proven its advantage in creating clinkerless binders [2], regulating the kinetics of grinding copper ore [3], and with dry and wet grinding [4]. To improve the efficiency of the electromagnetic mill, studies have been conducted aimed at tracking the movement of the working medium in the mill [5, 6]. To improve the design of the electromagnetic mill so as to reduce energy consumption, various mills design solutions were proposed, mainly to ensure a uniform magnetic field inside the unit's mixing chamber to reduce electric losses [7–11]. However, it should be noted that the effect of the magnetic field on the properties of the material being ground during the operation of the electromagnetic mill has not been studied in the scientific literature.

* Corresponding author: ibragimov@kgasu.ru

http://dx.doi.org/10.28991/CEJ-2023-09-05-015

There are sufficient large number of works devoted to the effect of the magnetic field on the structure and properties of solids [12–14]. Koplak et al. (2014) determined that 66% of all articles devoted to the effect of the magnetic field on crystal properties relate to magnetic fields with an induction of 0.1–0.9 T [15]. It is stated that the relative change in the physical properties of solids when exposed to a magnetic field, i.e., $\Delta I/I$, in weak fields (~0.1–1 T) is the same for a wide range of materials and amounts to ~ 5%. However, Alshits et al. (2010) studied the mobility of edge dislocations in NaCl and LiF crystals and recorded a decrease in the dynamic braking coefficient of dislocations by 4.5 times when exposed to an electron beam (pulsed magnetic field) [16]. The effect of a magnetic field reduces the microhardness in NaCl single crystals, but this process is reversible, with a relaxation time lasting up to 18 hours [14]. It has been established that exposure to a magnetic field changes the strength and plastic characteristics of materials [17, 18].

Morozov et al. (2019) consider the formation of an elastic-plastic wave in a nonequilibrium near-surface area when exposed to a pulsed electromagnetic field [19]. It is shown that a voltage wave is formed in two stages in this area. The magnetoplastic effect, discovered in 1987 by Alshits et al. (1987), is characterized by an increase in metal plasticity in a magnetic field, associated with the detachment of dislocations in a magnetic field from paramagnetic centers of impurity and their movement in the internal voltage field [20]. It is established that the microhardness tends to change from the threshold value of induction of magnetic field B = 0.1 T, which is due to the existence of an energy barrier, the excess of which leads to the detachment of dislocations from paramagnetic centers [21]. A decrease in yield strength σ_T is the reason for a decrease in microhardness in a magnetic field, according to the known ratio $\frac{H_m}{3} = \sigma_T$ [22]. This phenomenon, called strength degradation, is associated with the detachment of dislocations from paramagnetic centers, which are point stoppers. The relative change in the velocity of dislocations in a magnetic field is expressed by Equation 1 [23]:

$$\frac{\Delta v}{v_0} = \frac{1}{2}\frac{(U_S - U_{T0})}{kT}\left(\frac{B}{B_0}\right)^2 \quad (1)$$

(where v_0 is the average dislocation velocity; Δv– the change in the average dislocation velocity in the magnetic field; U_S and U_{T0}– the dislocation separation energy from the paramagnetic impurity in the singlet and triplet states of the "radical pair": the electron spin in the dangling bond of the dislocation core and the electron spin of the paramagnetic impurity; B– the magnetic induction vector of the external magnetic field; B_0– the saturation field, that is a characteristic parameter for this material; k– Boltzmann's constant; T–temperature), which demonstrates that, other things being equal, an increase in magnetic induction has a strong effect on the mobility of dislocations. The accumulation of defects in the material under magnetic field when the material is being machined under the effect of a magnetic field (activation) should not only change the geometric characteristics of the particles of the material being processed, but also the physical and chemical properties of the surface layer of particle material.

Kotov et al. (2000) shows that with electromagnets introduced into the ball mill casing, one could significantly increase the efficiency of ore grinding by controlling the movement pattern of metal balls [24]. Egorov et al. (2017) found that when processing a dispersed medium in a magnetically liquefied layer, grinding process becomes more intensive compared to the grinding in a hammer mill without exposure to electromagnetic field for the same period of time, accompanied by a decrease in coherent scattering areas and the formation of additional micro-deformations [25]. Meanwhile, there is no information about the influence of the magnetic field value on the fracture velocity of the ground material. In the majority of scientific works magnetic field is considered as a factor of influence on the stability of cement grout [26], in estimating of the cement hydration [27], either in the production of the magnetic cement [28] thus, there are no approaches to determination the impact of the magnetic field on the ground medium in the vortex mill.

The presented analysis of scientific and technical information indicates that when grinding materials in machines that use an electromagnetic field, the effects that contribute to this field being destructive to the processed material should be observed. The purpose of this work is to determine the effect of the magnetic field on the strength of cement stone and the kinetics for grinding portland cement in a mill when exposed to a magnetic field. This paper adopts a working hypothesis that the electromagnetic field contributes to the accumulation of dislocations in the material, an acceleration of their movement, the development of cracks (as one of the aspects of the magnetoplastic effect).

2. Materials and Methods

2.1. The Determination of Portland Cement Dispersion

In order to achieve these objectives, the research consists of two consecutive phases. At the first phase of the research the characteristics of dispersion properties of portland cement processed by the vortex layer device were determined.

During the test, CEM I 42.5 B portland cement (Novotroitsk, Russia) was used, as per the requirements of EN 197-1. The specified portland cement has the following mineralogical composition: C_3S – 64-65%, C_2S – 11-13%, C_3A – 5-6%, C_4AF – 14-15%. The plasticizer Melflux 2651 F (hereinafter referred to as ML) was used as an additive – a chemical additive based on polyether carboxylate (the polymer chain is formed by α, β–unsaturated carboxylic acids), a 400-600 kg/ m^3 bulk density powder, produced by BASF concern.

A mixture of Portland cement and plasticizer was mechanically activated in a 297 vortex layer device (VLD) manufactured by Regionmettrans LLC (see Figure 1). The method for processing portland cement in VLD is shown in [11]. The maximum processing time of portland cement was 8 minutes. VLD generates a rotating magnetic field that drives metal rods to grind portland cement powder.

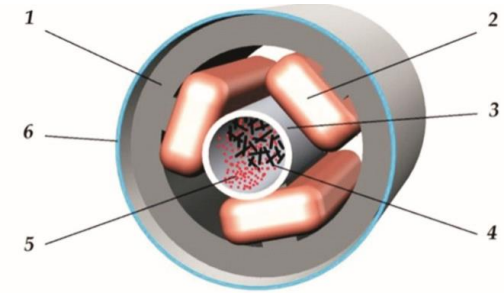

Figure 1. Typical structure of a rotating electromagnetic field machine: 1– inductor's magnetic core; 2 – inductor's three-phase coil; 3 – non-magnetic cylindrical case of the machine's working body; 4 – ferromagnetic needles; 5 – the material processed; 6 – the cover.

The granulometric composition of the dispersed Portland cement powder was evaluated using a HORIBALA-950 laser particle size analyzer. The specific surface area was evaluated by the air permeability method with a PSX-9 device and the BET method (using Nova 1200e Quantachrome analyzer). The distribution of the size of the portland cement particles during VLD crushing is determined.

2.2. The Determination of the Impact of Magnetic Field on Cement Stone Strength at Axial Tension

In the second phase of the study, the magnetic field's effect on the strength of cement stone was determined. To this end, two types of cylindrical samples were made: type 1: 300 mm long and 46 mm in diameter; type 2: 241 mm long and 37 mm in diameter. The specimens were made out of cement paste mixture with a water-cement ratio of 0.2. Each type of sample has a total of 60 pcs. The filler was not used in order to exclude the effect of the filler contacting the cement stone. Plasticizer ML was used in the amount of 1% of the total mass of portland cement.

For the purpose of simulating the effect of the magnetic field on the strength of cement stone, an inductance coil was designed. In this case, the value of the magnetic field induction inside the coil should be approximately equal to the value of the induction inside the working chamber of the vortex intensifier (0.2-0.3 T), used for mechanical activation of portland cement. The parameters of the coil were determined by preliminary calculations. Designed for experimental research, the inductance coil is made of PET 155 copper wire with a cross–sectional area of 1.5 mm^2 with 16,000 turns and has the following geometric characteristics: length of 135 mm, winding thickness of 50 mm, inner diameter of 46.5 mm. The value of the magnetic induction was tested by a magnetometer equipped with a ZMST-5 Hall sensor. The connection diagram of the coil and its exterior view are shown in Figures 2-a and 2-b.

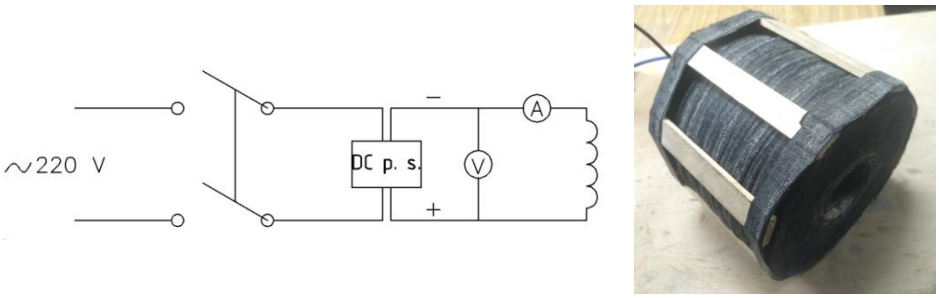

(a) (b)

Figure 2. a-Coil connection diagram; b-exterior view of the assembled coil

Experiments were conducted with the following testing equipment. Universal test machines IR 5082-5 and IR 5082 with pneumatic or manually operated grips and an electromechanically operated middle crosshead. Deformations of specimens during the tests are measured directly and indirectly, directly with an extensometer and indirectly with the measurement of middle crosshead displacement. Specimens can be tested for flexural load, tension, and compression. The testing machine is operated by a PC that also collects and analyzes the obtained data.

Some specimens that required additional measurements of some additional parameters, such as strain, were tested in a testing machine connected to a tensiometry equipment NI cDAQ9188 chassis and NI 9219 modules connected to the

additional PC. The strains during the test were monitored in real time with NI LabView software, which also conducted data acquisition and analysis. Data obtained from the testing machine PC and tensiometry PC were merged and synchronized for further analysis. Samples of each type have been tested for axial extension under and without magnetic fields (30 samples per series). The results of the obtained data dependencies are as follows: voltage and relative deformation.

The relative deformation value is eliminated by a tension sensor on the extended surface in the middle of the sample along the load application. The values were removed at each step before and after applying the load to the sample, and the average value was calculated. Based on the test data, dependency diagrams between relative deformations and the applied sample loads were constructed. Later, the diagrams were analyzed according to criteria accepted by the authors, such as deformation growth rate, straightness of the sections of the ascending and descending branches, and curvature of the diagram. An analysis of the diagram is shown in the text section of the article.

SEM tests of the obtained cement stone specimens were made out using an electron microscope consisting of an AZtec X-MAX energy dispersion spectrometer. With the resolution of the spectrometer being 127 eV, the first stonestone was alloy Au/Pd in the ratio 80/20 on the turbomolecular pumped coater T150 ES, and after that, the surface was shot at an accelerating voltage of 5 keV. The main parameters of the experiment are an accelerating voltage of 20 keV, a working segment of 9 mm, and a sound depth of sounding less than 1 lm. Following the axial tension tests, the cleavage of the specimen surface was tested using a Multimode V scanning (research) probe microscope with an electrochemical adaptor installed.

3. Results and Discussions

3.1. Effect of the Magnetic Field on The Dispersion Kinetics of Portland Cement

To evaluate the effect of the electromagnetic field on the destruction of non-magnetic material particles, which include Portland cement, changes in its dispersed composition were tested after it had been processed in a vortex intensifier. The variable processing parameters were as follows: the processing duration and the value of magnetic induction inside the working chamber of the equipment. The measurement data of the magnetic field induction inside the vortex intensifier's chamber along the opposite poles is shown in Figure 3-a. The inductor magnetic field is characterized by an intensity that does not depend on the nature of the medium, but is determined only by the geometric dimensions of the circuit and the value of the current (A/m). For a salient-pole inductor, the dependence of magnetic induction on the current consumed by the inductor windings is shown in Figure 3-b.

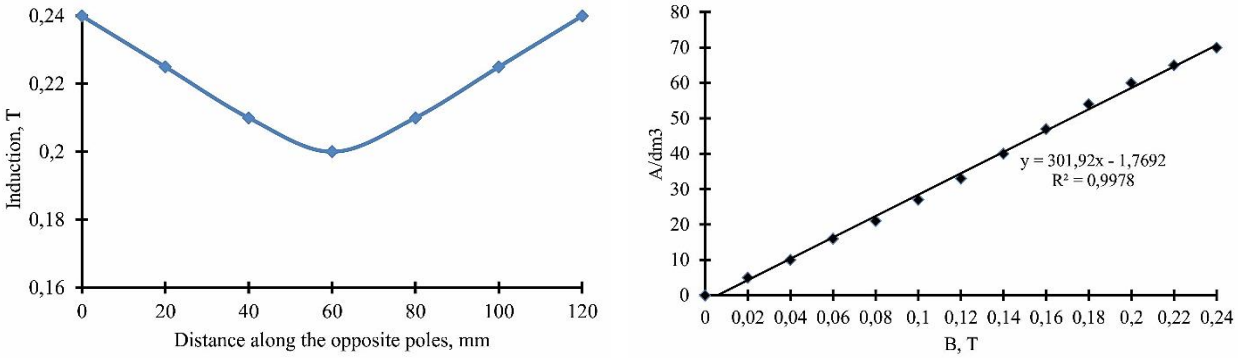

(a) (b)

Figure 3. a-Distribution of the measured value of magnetic induction inside the working chamber along the line between opposite poles; b-The value of the required current consumed by the inductor windings to produce necessary induction in the center of its bore hole.

Figure 3 shows that the lowest value of magnetic field induction (0.2 T) is in the center of the working chamber, which increases from the center to the edge. It is assumed that the induction of the magnetic fields depends on the current force of the inductors' windings, which is linear. It has been established that a significant amount (up to 48%) of the vortex layer's power is converted into heat, with no more than 35% used for the mixing and grinding processes [3, 4]. When ferromagnetic elements interact with each other and the slip bushing, a voltage difference (up to 17 mV) is produced, having intermittence with a frequency of 4...10 microseconds. This leads to an electrolytic effect in electrically conductive media, with up to 15% of the vortex layer's power used for electrolysis and only about 2% of the energy spent on producing a high-frequency magnetic field and acoustic vibrations in the medium [5–9]. The magnetic field induction modulus on the circular current axis at a distance z from its center is determined by the Biot-Savart law:

$$B = \frac{\mu\mu_0 I R^2}{2(R^2+z^2)^{3/2}}, \quad (2)$$

where μ is the magnetic permeability of the material, $\mu_0 = 4 \cdot \pi \cdot 10\text{-}7$Gn/m is the magnetic constant, I is the current rate in the wire, R is the radius of the circular current, z is the distance from the center of the circular current. In accordance with Equation 2, a graph of the magnetic field induction distribution inside a coil designed for experimental studies is constructed, where the abscissa axis is the length of the coil (m) (Figure 4).

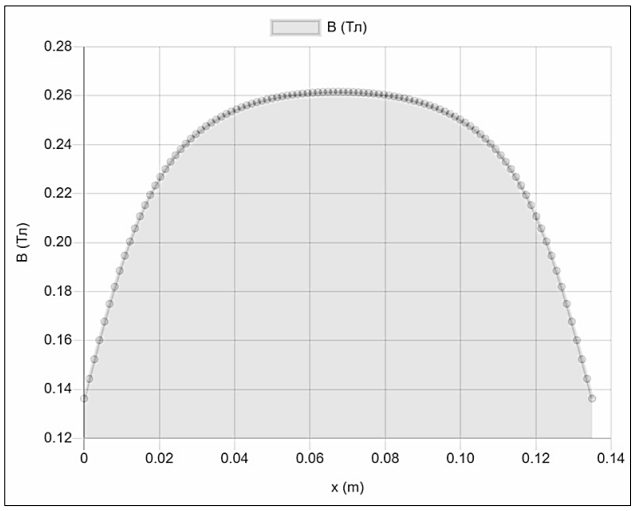

Figure 4. Distribution of magnetic field induction inside the experimental coil

The obtained maximum value of the magnetic field induction inside the coil, equal to 0.26 T, is confirmed by measurements using a Hall sensor magnetometer. Thus, the obtained value is almost identical to the magnetic field induction value of the VLD working chamber. The effect of the vortex intensifier processing duration on the dispersed composition of Portland cement particles is shown in Figure 5.

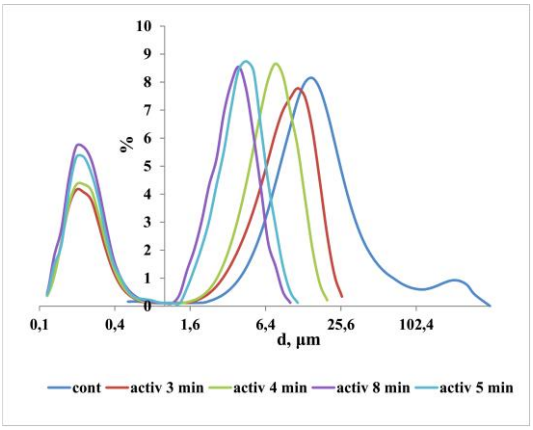

(a)

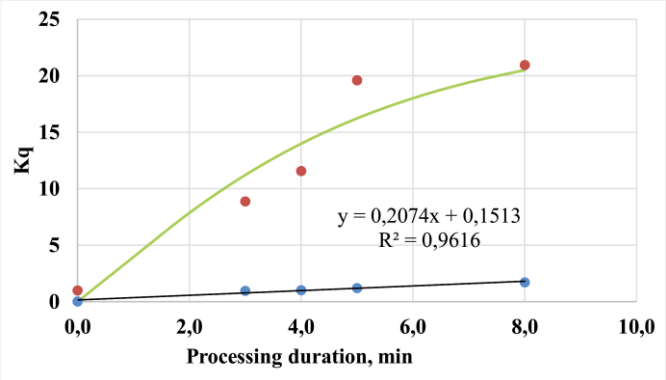

(b)

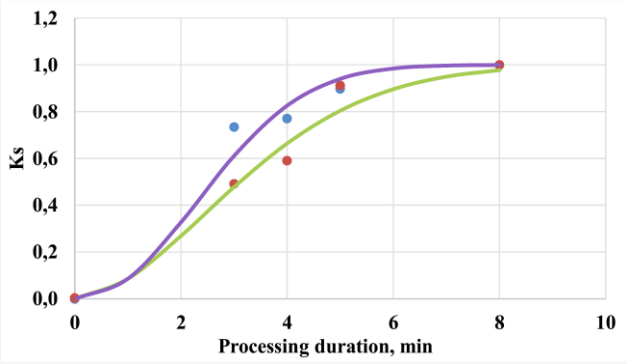

(c)

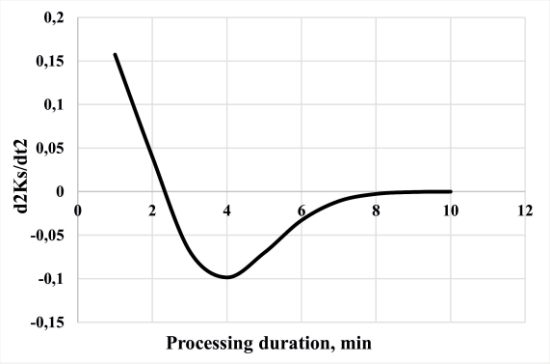

(d)

Figure 5. a- the dependence of the granulometric composition on the portland cement particles processing duration in VLD; b- the dependence of the indicator K_q on the portland cement particles processing duration in VLD; c- the dependence of the indicator K_S on the portland cement particles processing duration in VLD; d- The dependence of the indicator acceleration K_S on the portland cement particles processing duration in VLD.

The data presented in Figure 5 demonstrate that an increase in the processing duration in VLD leads to a significant change in the dispersed composition of the Portland cement powder: a pronounced polymodality of the particle distribution is observed, with an increase in the first mode located in the small particle region (0...2 microns) and a decrease in the second mode located in the region of particles larger than 2 microns. A detailed analysis of the dispersed distribution of Portland cement particles was carried out using the following criteria:

- Reduced particles fraction for the mode within the range of particle sizes:

$$K_q = \frac{\left(d_{max,i}(t) - d_{min,i}(t)\right)_{max}}{d_{max,i}(t) - d_{min,i}(t)} \times \frac{Q_i(t)}{Q_{i,max}} \quad (3)$$

- Reduced specific surface area of the mode particles:

$$K_S = \frac{S_i(t)}{S_{max}} \quad (4)$$

where $i$is the mode number ($i = 1, 2$); t– processing duration in VLD; $Q_i(t)$– the total particle content of the corresponding mode; $Q_{i,max}$– the maximum total particle content of the corresponding mode; $d_{max,i}(t)$and $d_{min,i}(t)$– respectively, the maximum and minimum diameter of the mode particles; $\left(d_{max,i}(t) - d_{min,i}(t)\right)$ – the maximum range of particle diameters in the entire range of portland cement particles processing duration in VLD; $S_i(t)$– the specific surface area of the particles of the corresponding mode S_{max}– the maximum specific surface area of the particles of the corresponding mode in the entire processing range in VLD.

Distribution data analysis for Portland cement particles (Figure 5-a) shows that the criterion $K_q$for the first (highly dispersed) mode in the investigated range of processing time is confined to a linear law with high determination coefficient $R^2 = 0{,}96$ (Figure 5-b). This behavior is caused by both an increase in the total content of highly dispersed particles and a decrease in the range of particle diameters. The main feature is the proportionality of variations in these values within the investigated range of Portland cement particles processing duration in VLD.

The variation in the second mode has a different form: the indicator value tends to saturate$K_q(t)$. By comparing the values of the indicators K_q for the first and second modes we can see that they differ by an order of magnitude. This indicates a more significant change in the same indicator for the second mode, which is associated with a small variation in the particle diameter range, which compensates for the decrease in the total particle content for this mode.

The dependence of the indicator K_S (which is more self-explanatory) on the portland cement particles processing duration in VLD has a more complex pattern of variation with saturation and is described by a function of the form

$$K_S = 1 - exp\left(-\alpha t^{\theta}\right) \quad (5)$$

where $\alpha$and $\theta$are empirical coefficients, the values of which are given in Table 1: α is a coefficient characterizing the increase rate of the reduced specific surface area of particles; θ is a coefficient characterizing the rate of deceleration of the reduced specific surface area of particles.

Table 1. Values of empirical coefficients $K_S = 1 - exp\left(-\alpha t^{\theta}\right)$

Mode	Empirical coefficients	
	α	θ
Mode I	0.09	1.80
Mode II	0.09	2.14

Data analysis in Figure 5-b and Table 1 shows that an increase in the processing time in VLD leads to an increase in $K_S$both the first and second modes indicators. At the same time, the braking coefficient of the second mode is θ lower (by 19%), which indicates a higher rate of transition of this mode particles to a more dispersed state (the first mode). In addition, the given saturation (which is probably characteristic property of the vortex intensifier and ferromagnetic bodies used) indicates the possibility of selecting the optimal mode in terms of its efficiency, that is, achieving a high specific surface area of particles with a minimum processing time required. To do this, it is enough to accept:

$$\frac{d^2 K_S}{dt^2} = min \quad (6)$$

Figure 5-d shows that the specified condition corresponds to the process duration lasting $t = 4$ minutes. Thus, the VLD's effective processing time for portland cement is 4 minutes. The data obtained match the conclusion that the effective activation time in the electromagnetic mill is 3-7 min [8-10].

3.2. Effect of the Magnetic Field on the Strength of Cement Stone

The cylindrical samples were tested for axial tension both without the influence of magnetic field and under the influence of magnetic field (MF) (Figure 6). The magnetic field is generated by an experimental coil shown in Figure 2. The results of the axial tension test of the cylindrical samples are shown in Table 2.

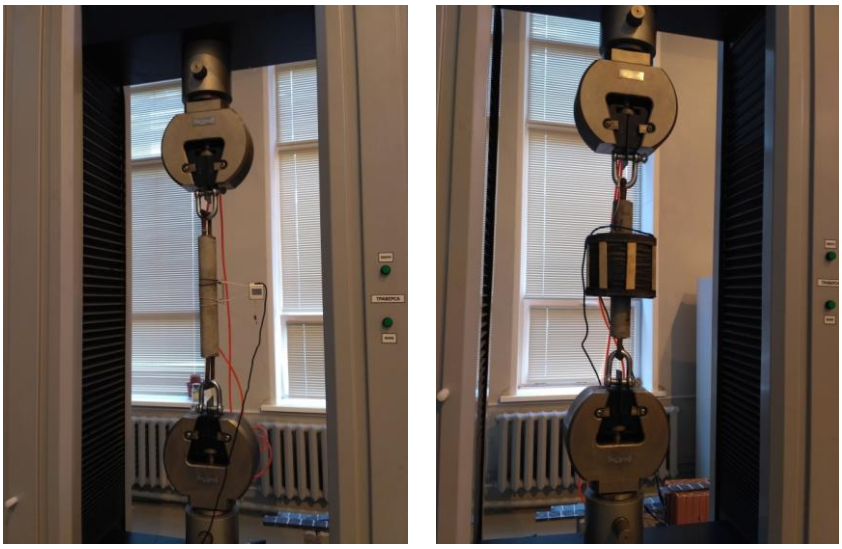

(a) (b)

Figure 6. Testing scheme: A – without the effect of a magnetic field; B – when exposed to a magnetic field created by the coil

Table 2. Axial tensile test results

No. item	F_1, kN	R_{bt1}, MPa	F_2, кН	R_{bt2}, MPa	No. item	F_3, кН	R_{bt3}, MPa	F_4, кН	R_{bt4}, MPa
1	1.93	1.16	0.72	0.43	31	0.96	0.89	0.46	0.43
2	1.88	1.13	0.77	0.46	32	0.99	0.92	0.44	0.41
3	1.95	1.17	0.75	0.45	33	0.94	0.87	0.39	0.37
4	1.88	1.13	0.76	0.46	34	1.01	0.94	0.42	0.39
5	1.91	1.15	0.77	0.47	35	0.83	0.77	0.35	0.33
6	1.86	1.12	0.76	0.45	36	0.91	0.85	0.38	0.35
7	1.86	1.12	0.78	0.47	37	0.84	0.79	0.34	0.32
8	1.86	1.12	0.75	0.45	38	0.80	0.74	0.38	0.35
9	1.86	1.12	0.80	0.48	39	0.85	0.79	0.41	0.38
10	2.03	1.22	0.78	0.47	40	0.87	0.81	0.37	0.34
11	1.88	1.13	0.77	0.46	41	0.77	0.72	0.42	0.39
12	1.86	1.12	0.75	0.45	42	0.76	0.70	0.39	0.37
13	1.69	1.02	0.80	0.48	43	0.89	0.82	0.37	0.34
14	1.69	1.02	0.77	0.46	44	0.74	0.69	0.39	0.36
15	1.86	1.12	0.80	0.48	45	0.83	0.77	0.42	0.39
16	1.69	1.02	0.75	0.45	46	0.78	0.72	0.43	0.40
17	1.91	1.15	0.77	0.46	47	0.83	0.78	0.37	0.34
18	1.93	1.16	0.78	0.47	48	0.83	0.77	0.41	0.38
19	1.69	1.02	0.74	0.44	49	0.75	0.70	0.42	0.39
20	1.88	1.13	0.78	0.47	50	0.85	0.79	0.39	0.37
21	1.86	1.12	0.74	0.44	51	0.78	0.72	0.40	0.37
22	1.88	1.13	0.77	0.46	52	0.85	0.79	0.38	0.36
23	1.91	1.15	0.76	0.45	53	0.88	0.82	0.40	0.37
24	1.88	1.13	0.77	0.46	54	0.85	0.79	0.37	0.35
25	1.86	1.12	0.74	0.44	55	0.82	0.76	0.37	0.35
26	1.86	1.12	0.76	0.45	56	0.93	0.87	0.38	0.36
27	1.86	1.12	0.77	0.46	57	0.84	0.78	0.38	0.35
28	1.88	1.13	0.74	0.44	58	0.84	0.78	0.40	0.37
29	1.88	1.13	0.80	0.48	59	0.81	0.76	0.39	0.36
30	1.86	1.12	0.77	0.46	60	0.86	0.80	0.40	0.37
	R_{bt1} = 1.1 ± 0.1		R_{bt2} = 0.46 ± 0.02			R_{bt3} = 0.94 ± 0.15		R_{bt4} = 0.36 ± 0.05	

Table 2, R_{bt1} and R_{bt2} shows the axial tensile strength of type 1 specimens (300 mm long and 46 mm in diameter) with and without exposure to the magnetic field generated by the coil, respectively; R_{bt3} and R_{bt4} are the axial tensile strength of type 2 specimens (241 mm long and 37 mm in diameter) with and without exposure to the magnetic field generated by the coil, respectively; F_n is the breaking force.

Figures 7 and 8 show averaged diagrams "stress – relative deformations".

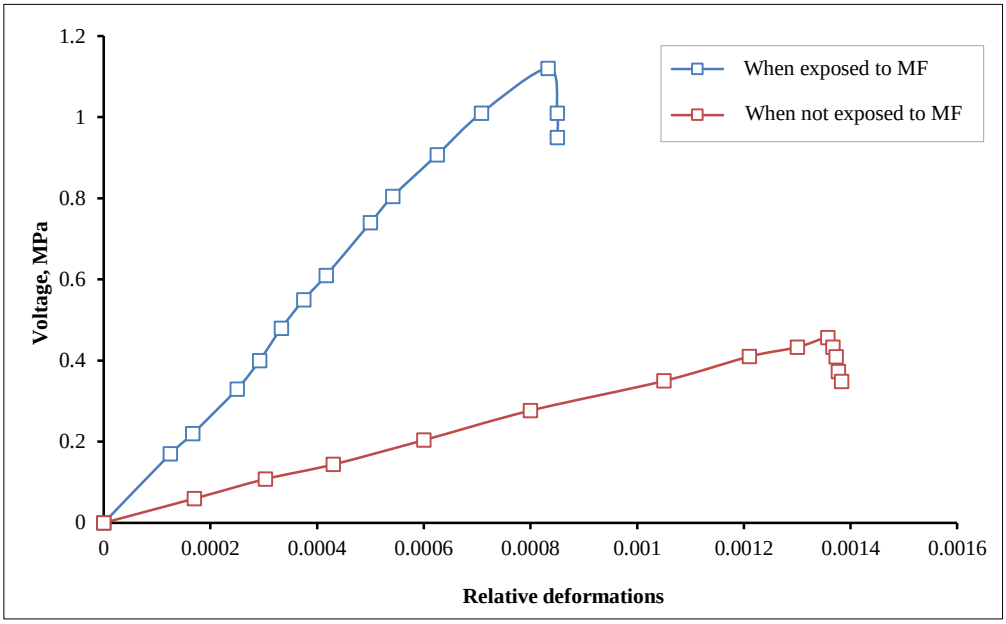

Figure 7. Diagram "stress – relative deformations" of type 1 specimens

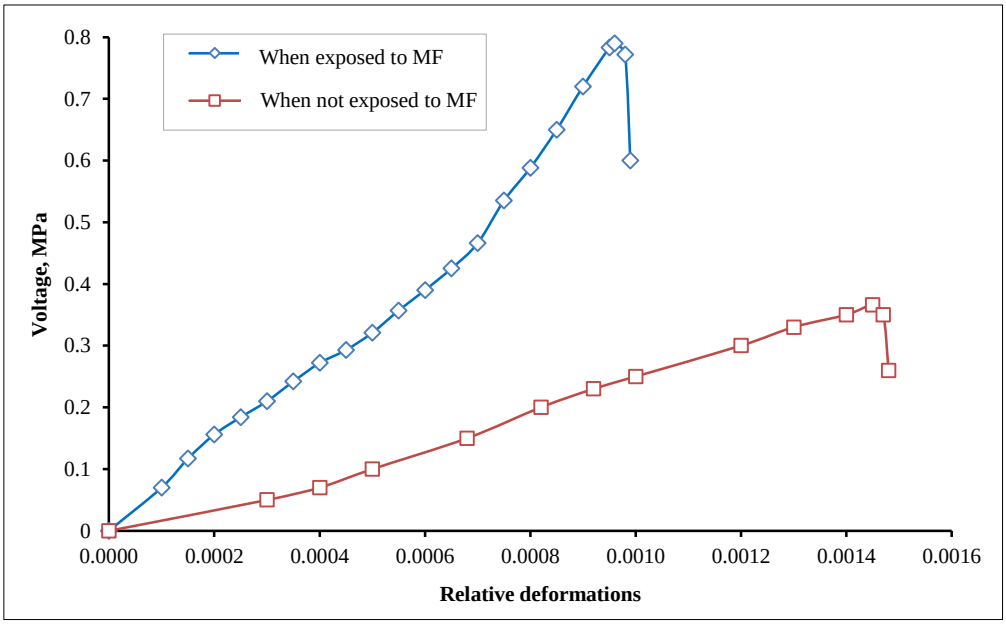

Figure 8. Diagram "stress – relative deformations" of type 2 specimens

The data in Table 2 shows that the effect of a magnetic field reduces axial tensile strength. Moreover, with the cross-sectional area of the specimens decreasing, the effect of the magnetic field is more significant. Thus, for type 1 specimens (diameter 46 mm), the effect of a magnetic field reduces axial tensile strength by 17%, and for type 2 specimens (diameter 37 mm), axial tensile strength is decreased by 28%. By comparing the values of axial tensile strength reduction with the ratio of the cross-sectional areas of the specimens of the said types, $S_1/S_2 = 1.55$, one could suggest that the effect of the magnetic field is localized in the surface layers of the specimens.

The diagrams "axial tension – relative deformations" ("$\sigma - \varepsilon$") show the presence of a magnetoplastic effect: for type 1 specimens, relative deformations are increased by 65%, as compared to the specimens tested with no exposure to a magnetic field, for type 2 specimens' relative deformations are increased by 51%. Naturally, in accordance with the Mises–Hencky theory [29] (the energy theory of the limit state of deformable material), this leads to a change in energy consumption for deformation and destruction of cement stone:

$$U_{tot} = U_d + U_f \quad (7)$$

where U_{tot} is is the total energy consumption for material's resistance to the external load; U_d is energy consumption for material's deformation; U_f is energy consumption for material's destruction with new surfaces formed. The values included in Equation 7 can be determined by the area of the diagram "σ-ε" [30]:

$$U_{tot} = \int_0^{\varepsilon} \sigma_{bt}(\varepsilon) d\varepsilon \quad (8)$$

Values calculation data U_{tot}according to the Equation 8 are shown in Table 3. According to Table 3 it can be seen that the energy consumption for type 1 cement stone specimens' deformation and destruction when exposed to MF is decreased by 33%, and for type 2 specimens – by 30%. The data obtained improve and supplement the idea of reduction the resistance of solids under the influence of magnetic field for crystals and polymers [15, 16, 18].

Table 3. Energy consumption for deformation and destruction of cement stone under tension

Specimen type	U_{tot} without exposure to MF	U_{tot} when exposed to MF
1	0.93	0.62
2	0.73	0.51

Note: Units of measurement for the values included in the table: kJ/m^3.

Having processed the data shown in Figures 7 and 8 using the formulas:

$$\sigma_j = \frac{\sigma_{max}}{\sigma_i};\ \varepsilon_j = \frac{\varepsilon_{max}}{\varepsilon_i} \quad (9)$$

where σ_j and ε_j are the relative values of stresses and deformations, we obtain the diagrams shown in Figure 9.

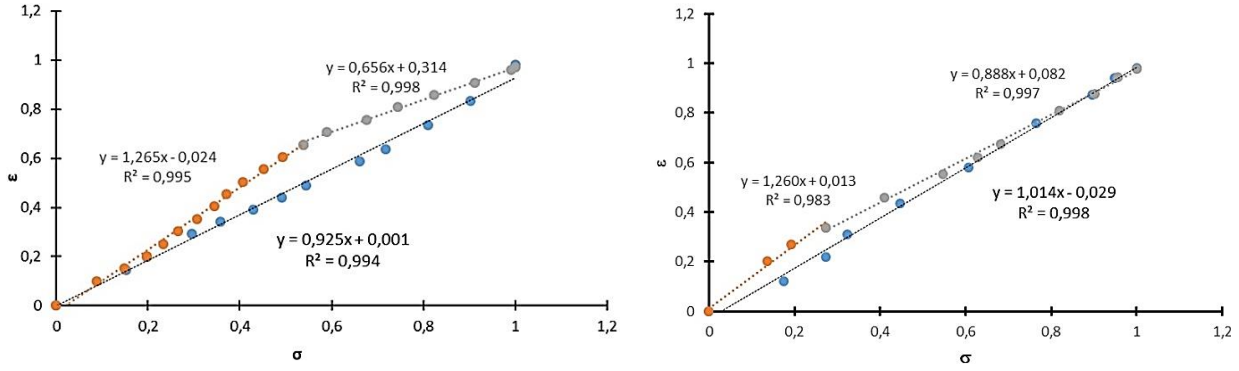

(a) (b)

Figure 9. Diagrams "$\sigma_{rel} - \varepsilon_{rel}$" in relative coordinates: a) for type No. 1 and 2 specimens without exposure to a magnetic field; b) for type No. 1 and 2 specimens when exposed to a magnetic field

The analysis of these diagrams, given in relative coordinates (Figure 9), with the exception of the descending branch of the diagram, allows us to identify some features of the magnetic field effect. Regardless of the effect of the magnetic field, the presence of a change point in the deformation rate for type 2 specimens is a common feature. It was found that after being exposed to a certain load, the specimen's deformation rate decreases: without the effect of a magnetic field, by 52%, and when exposed to a magnetic field, by 71%. It is difficult to attribute this fact solely to the deformation of the test installation units. The reasons for this are: 1) the absence of this fact for type No. 1 and 2 specimens; and 2) the displacement of the change point coordinates in the deformation rate under the effect of a magnetic field.

The displacement of the change point in the specimens' deformation rate, which is a distinctive feature of the magneto plastic effect, in relative coordinates for the abscissa axis is $\Delta\sigma = 0.27$, which is equal to 50% relative to the abscissa of the specified point for the diagram "$\sigma_{rel} - \varepsilon_{rel}$" without the effect of a magnetic field. The ordinate of the change point in the deformation rate has also changed – by $\Delta\varepsilon = 0.32$ or 48% with respect to the ordinate of the specified point in the diagram "$\sigma_{rel} - \varepsilon_{rel}$" without the effect of a magnetic field. At the same time, it is obvious that the energy consumed for deformation in order to reach the change point in the deformation rate is decreased significantly by 3.9 times.

It is also important to note that the magnetic field affects the deformation rate in the second section of the diagram "$\sigma_{rel} - \varepsilon_{rel}$" (after the change point in the deformation rate). For the first section, the values of the coefficient of $k$linear dependencies $\varepsilon_{отн} = k\sigma_{отн} + b$shown in Figure 9 both with and without a magnetic field applied are approximately equal (the difference is less than 0.4%). For the second sections of the diagram "$\sigma_{rel} - \varepsilon_{rel}$", the coefficients $k$have different values: the deformation of the cement stone specimen when exposed to MF increases by 35% (from $k = 0.656$to$k = 0.888$). The external magnetic field of cement stone samples changes the deformation and fracture rate process, especially in compressed granite samples [31-33].

The magnetoplastic effect can be visually seen as a change in the nature of the crack edges' surface (Figure 10). The nature of the crack surface in the cement stone deformed with no magnetic field applied has a classic nature: extended relatively smooth areas have cracking development after exposure to a load of a specific limit value; the relative fraction of the crack surface, typical for plastic deformation, is insignificant (Figure 10-c). The crack edge surface of the cement stone, which was exposed to a magnetic field during the test, is significantly different. Not only has the area of the cracking development changed (it decreases multiple times), but so has the nature of its development (Figure 10-d). The development of several "steps", which lead to the formation of a cracking area, can be identified. Therefore, the external impact of the magnetic field on exposed samples causes a displacement effect and cracks. The installed effect complements the data obtained from pure crystals [34–37].

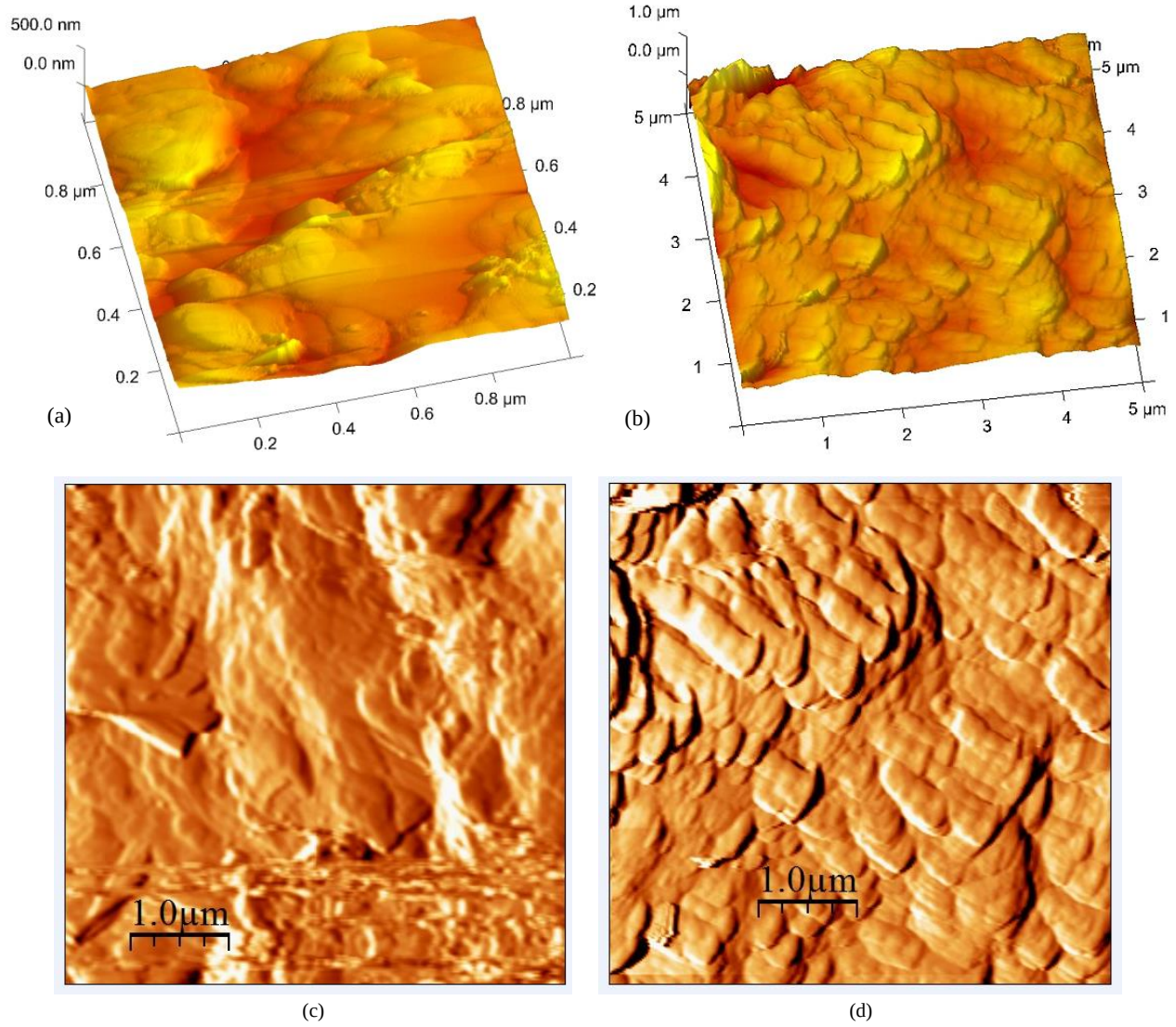

Figure 10. Chipping of specimens' surfaces after testing: a, c without the effect of a magnetic field in 3D and 2D images; b, d- when exposed to a magnetic field in 3D and 2D images, respectively

This result is a visual representation of the validity of the hypothesis put forward, namely the hypothesis on the effect of the magnetic field on the properties of polycrystalline materials, in particular Portland cement and cement stone.

4. Conclusion

According to theoretical and experimental research, it was found that the effect of a magnetic field on cement stones was to reduce their strength by accumulating structural defects, electro-dislocation interactions between defects, and cracks in the mouth and borders. There is not only a change in the area of crack growth (decomposed into folds), but also in its form of "steps" formation, which culminates in the formation of the crack location.

The external behavior of the magnetic field in tensile stresses on cement stone increases relative deformations by 51 to 65% and the deformation rate. The effect of magnetic fields is more significant with the reduction in the sample's cross-section. The energy costs of breaking cement composites under magnetic field influence were reduced by 30 to 33%.

The granulometric composition of Portland cement crushed in the electromagnetic mill has a two-mode distribution. At the same time, the total number of fine-dispersed particles has increased, and the range of variation in particle diameter has decreased in relation to the treatment length of the vortex layer device.

Therefore, magnetic fields affect the stress-strain state of the material, reduce its strength, increase the rate of development, and increase the absolute values of plastic deformations. The established effect of magnetic fields on polycrystalline materials with isotropic structures (cement stone) can be used in the processing technology of concrete waste to reduce its grinding costs.

5. Declarations

5.1. Author Contributions

Conceptualization, R.I. and E.K.; methodology, E.K.; software, L.G.; validation, R.I., E.Kh., and L.G.; formal analysis, E.K.; investigation, R.I.; resources, R.I.; data curation, E.Kh.; writing—original draft preparation, R.I.; writing—review and editing, E.K.; visualization, E.Kh.; supervision, E.K.; project administration, R.I.; funding acquisition, R.I. All authors have read and agreed to the published version of the manuscript.

5.2. Data Availability Statement

The data presented in this study are available on request from the corresponding author.

5.3. Funding

The authors received no financial support for the research, authorship, and/or publication of this article.

5.4. Conflicts of Interest

The authors declare no conflict of interest.

6. References

[1] Khozin, V. G., Khokhryakov, O. V., Sibgatullin, I. R., Gizzatullin, A. R., & Kharchenko, I. J. (2014). Carbonate cements of low water-need is a green alternative for cement industry of Russia. Construction Materials, (5), 76-82.

[2] Khaydarov, B., Suvorov, D., Pazniak, A., Kolesnikov, E., Gorchakov, V., Mamulat, S., & Kuznetsov, D. (2018). Efficient method of producing clinker-free binding materials using electromagnetic vortex milling. Materials Letters, 226, 13–18. doi:10.1016/j.matlet.2018.05.016.

[3] Wołosiewicz-Glab, M., Pięta, P., Foszcz, D., Ogonowski, S., & Niedoba, T. (2018). Grinding kinetics adjustment of copper ore grinding in an innovative electromagnetic mill. Applied Sciences (Switzerland), 8(8). doi:10.3390/app8081322.

[4] Ogonowski, S., Wołosiewicz-Głąb, M., Ogonowski, Z., Foszcz, D., & Pawełczyk, M. (2018). Comparison of Wet and Dry Grinding in Electromagnetic Mill. Minerals, 8(4), 138. doi:10.3390/min8040138.

[5] Makarchuk, O., Calus, D., & Moroz, V. (2021). Mathematical Model to Calculate the Trajectories of Electromagnetic Mill Operating Elements. Tekhnichna Elektrodynamika, 2021(2), 26–34. doi:10.15407/techned2021.02.026.

[6] Całus, D., & Makarchuk, O. (2019). Analysis of interaction of forces of working elements in electromagnetic mill. Przeglad Elektrotechniczny, 95(12), 64–69. doi:10.15199/48.2019.12.12.

[7] Milykh, V. I., & Tymin, M. G. (2021). A comparative analysis of the parameters of a rotating magnetic field inductor when using concentric and loop windings. Electrical Engineering and Electromechanics, 4(4), 12–18. doi:10.20998/2074-272X.2021.4.02.

[8] Wołosiewicz-Głąb, M., Ogonowski, S., & Foszcz, D. (2016). Construction of the electromagnetic mill with the grinding system, classification of crushed minerals and the control system. IFAC-PapersOnLine, 49(20), 67–71. doi:10.1016/j.ifacol.2016.10.098.

[9] Wolosiewicz-Glab, M., Ogonowski, S., Foszcz, D., & Gawenda, T. (2018). Assessment of classification with variable air flow for inertial classifier in dry grinding circuit with electromagnetic mill using partition curves. Physicochemical Problems of Mineral Processing, 54(2), 440–447. doi:10.5277/ppmp1867.

[10] Ogonowski, S., Ogonowski, Z., & Swierzy, M. (2017). Power optimizing control of grinding process in electromagnetic mill. Proceedings of the 2017 21st International Conference on Process Control, PC 2017, 370–375. doi:10.1109/PC.2017.7976242.

[11] Shvedchykova, I., Melkonova, I., & Romanchenko, J. (2020). Research of magnetic field distribution in the working area of disk separator, taking into account an influence of materials of permanent magnets. EUREKA, Physics and Engineering, 2020(1), 87–95. doi:10.21303/2461-4262.2020.001106.

[12] Alshits, V. I., Darinskaya, E. V., Koldaeva, M. V., & Petrzhik, E. A. (2008). Dislocations in Solids. Elsevier, Amsterdam, Netherlands.

[13] Alshits, V. I., Darinskaya, E. V., Koldaeva, M. V., & Petrzhik, E. A. (2008). Chapter 86 Magnetoplastic Effect in Nonmagnetic Crystals. Dislocations in Solids, 14, 333–437. doi:10.1016/S1572-4859(07)00006-X.

[14] Golovin, Y. I. (2004). Magnetoplastic effects in solids. Physics of the Solid State, 46(5), 789–824. doi:10.1134/1.1744954.

[15] Koplak, O. V., Dmitriev, A. I., Alekseev, S. I., & Morgunov, R. B.. (2014). Universal regularities of the influence of a magnetic field on the properties of solids. Chemical Physics, 33(12), 18–23. doi:10.7868/s0207401x14120085.

[16] Alshits, V. I., Darinskaya, E. V., Morozov, V. A., Kats, V. M., & Lukin, A. A. (2010). ESR in the Earth's magnetic field as a cause of dislocation motion in NaCl crystals. JETP Letters, 91(2), 91–95. doi:10.1134/s0021364010020086.

[17] Dunin-Barkovskii, L. R., Morgunov, R. B. & Tanimoto, Y. (2005). The Influence of a Static Magnetic Field up to 15 T on the Manifestation of the Portevin–Le Chatelier Effect in NaCl : Eu Crystals. Physics of the Solid State, 47(7), 1282. doi:10.1134/1.1992606.

[18] Peschanskaya, N. N., & Sinani, A. B. (2008). Effect of the magnetic field on nanometer-scale deformation jumps in polymers. Physics of the Solid State, 50(1), 182–187. doi:10.1134/s1063783408010332.

[19] Morozov, V. A., Petrov, Y. V., & Sukhov, V. D. (2019). Experimental Evaluation of Structural and Temporal Characteristics of Material Fracture Based on Magnetic Pulse Loading of Ring Samples. Technical Physics, 64(5), 642–646. doi:10.1134/S1063784219050165.

[20] Alshits, V. I., Lyubimov, V. N., Sarychev, A. V., & Shuvalov, A. L. (1987). Topological characteristics of singular points of the electric field accompanying sound propagation in piezoelectrics. Soviet Physics—JETP, 66(2), 408-413.

[21] Al'shits, V. I., Darinskaya, E. V., Kazakova, O. L., Mikhina, E. Y., & Petrzhik, E. A. (1996). Magnetoplastic effect and spin-lattice relaxation in a dislocation-paramagnetic-center system. JETP Letters, 63(8), 668–673. doi:10.1134/1.567085.

[22] Golovin, Yu. I. (2004). Magnetoplastic effects in solids. Physics of the Solid State, 46(5), 789–824. doi:10.1134/1.1744954.

[23] Molotsky, M. I. (1991). A possible mechanism of magnetoplastic effect. Solid State Physics, 33(10), 3112-3114.

[24] Kotov, Y. A., Mesyats, G. A., Filatov, A. L., Koryukin, B. M., Boriskov, F. F., Korzhenevskii, S. R., Motovilov, V. A., & Shcherbinin, S. V. (2000). Complex processing of pyrite wastes from ore-dressing plants by nanosecond pulses. Doklady Earth Sciences, 373, 790–792. (In Russian).

[25] I Egorov, I. N., & Egorov, N. Ya. (2017). Influence of grinding conditions in a hammer mill on the efficiency of the process and the structural characteristics of the powder. International Research Journal, 11(65), 31-36. doi:10.23670/IRJ.2017.65.073.

[26] Hu, H. xiao, Deng, C., & Chen, W. (2022). The effect of magnetization conditions on the stability of cement grout. In Case Studies in Construction Materials (Vol. 16). doi:10.1016/j.cscm.2022.e01016.

[27] Kim, H. S., Park, D. W., Oh, G. H., & Kim, H. S. (2021). Non-destructive evaluation of cement hydration with pulsed and continuous Terahertz electro-magnetic waves. Optics and Lasers in Engineering, 138. doi:10.1016/j.optlaseng.2020.106414.

[28] Chuewangkam, N., Pinitsoontorn, S., & Chindaprasirt, P. (2019). Properties of NdFeB magnetic cement. Cement and Concrete Composites, 103, 204–212. doi:10.1016/j.cemconcomp.2019.05.010.

[29] Hlaváček, I., Chleboun, J., & Babuška, I. (2004). Chapter VIII Hencky's and deformation theories of plasticity. In North-Holland Series in Applied Mathematics and Mechanics, 241–279, Elsevier, Amsterdam, Netherlands. doi:10.1016/S0167-5931(04)80012-3.

[30] Радайкин, О., & Radaikin, O. (2019). Comparative Analysis of Various Diagrams of Concrete Deformation According to the Criterion of Energy Consumption for Deformation and Destruction. Bulletin of Belgorod State Technological University Named after. V. G. Shukhov, 4(10), 29–39. doi:10.34031/article_5db33945315bb4.76965991. (In Russian).

[31] Panteleev, I., Mubassarova, V., Damaskinskaya, E., Naimark, O., & Bogomolov, L. (2015). Influence of weak electric field on spatial-temporal dynamics of damage evolution during granite deformation. AIP Conference Proceedings. doi:10.1063/1.4932867.

[32] Ioffe, A. F. (1936). Report on the work of the Physico-Technical Institute. Uspekhi Fizicheskih Nauk, 16(7), 847–871. doi:10.3367/ufnr.0016.193607c.0847.

[33] Lapshin, O. V., Boldyreva, E. V., & Boldyrev, V. V. (2021). Role of Mixing and Milling in Mechanochemical Synthesis (Review). Russian Journal of Inorganic Chemistry, 66(3), 433–453. doi:10.1134/S0036023621030116.

[34] Jeong, J., & Voyiadjis, G. Z. (2022). A physics-based crystal plasticity model for the prediction of the dislocation densities in micropillar compression. Journal of the Mechanics and Physics of Solids, 167. doi:10.1016/j.jmps.2022.105006.

[35] Skogvoll, V., Angheluta, L., Skaugen, A., Salvalaglio, M., & Viñals, J. (2022). A phase field crystal theory of the kinematics of dislocation lines. Journal of the Mechanics and Physics of Solids, 166. doi:10.1016/j.jmps.2022.104932.

[36] Lindroos, M., Pinomaa, T., Ammar, K., Laukkanen, A., Provatas, N., & Forest, S. (2022). Dislocation density in cellular rapid solidification using phase field modeling and crystal plasticity. International Journal of Plasticity, 148, 103139. doi:10.1016/j.ijplas.2021.103139.

[37] Blaschke, D. N. (2019). Velocity dependent dislocation drag from phonon wind and crystal geometry. Journal of Physics and Chemistry of Solids, 124, 24–35. doi:10.1016/j.jpcs.2018.08.032.